

# Proximity to quantum criticality in the Ising ferromagnet $\text{TbV}_6\text{Sn}_6$

Tianxiong Han,<sup>1,2</sup> R. D. McKenzie,<sup>1,2</sup> Joanna Blawat,<sup>3</sup> Tyler J. Slade,<sup>1</sup> Y. Lee,<sup>1</sup> D. M. Pajerowski,<sup>4</sup> John Singleton,<sup>3</sup> Bing Li,<sup>4</sup> Paul C. Canfield,<sup>1,2</sup> Liqin Ke,<sup>1</sup> Ross McDonald,<sup>3</sup> Rebecca Flint,<sup>1,2</sup> and R. J. McQueeney<sup>1,2</sup>

<sup>1</sup>Ames National Laboratory, U.S. DOE, Iowa State University, Ames, Iowa 50011, USA

<sup>2</sup>Department of Physics and Astronomy, Iowa State University, Ames, Iowa 50011, USA

<sup>3</sup>National High Magnetic Field Laboratory, Los Alamos National Laboratory, Los Alamos, NM 87545

<sup>4</sup>Oak Ridge National Laboratory, Oak Ridge, TN, 37831, USA

(Dated: December 4, 2024)

$\text{TbV}_6\text{Sn}_6$  is a topological metal where ferromagnetic Tb ions with strong uniaxial magnetic anisotropy interact with V kagome layers. Inelastic neutron scattering measurements show that the Tb ions adopt an Ising doublet ground state. Here, we consider whether a transverse magnetic field can drive  $\text{TbV}_6\text{Sn}_6$  towards a quantum critical point, providing a rare example of transverse-field Ising criticality in a metallic compound. High-field magnetization measurements suggest that this quantum criticality is avoided and reveal a first-order-like spin-reorientation transition at 25.6 T due to an excited-state level crossing. Theoretical analysis shows that small changes in the local Hamiltonian can restore the quantum criticality for some in-plane field directions, suggesting that  $\text{TbV}_6\text{Sn}_6$  is close to a novel quantum tricritical point induced by in-plane magnetic anisotropy.

Kagome metals provide a promising platform for discovering topological and flat band physics with recent reports of charge-density wave order [1–4], superconductivity [5–7], itinerant magnetism [8–12], and Chern insulating phases [13–16]. Among the many kagome metal systems,  $RT_6X_6$  (166) systems with  $R$  = rare-earth,  $T$  = V, Cr, Mn, and  $X$  = Sn, Ge are unique for their combination of magnetic  $R$  ions that interact with metallic kagome  $T$  layers [17–19].

Particularly noteworthy is  $\text{TbV}_6\text{Sn}_6$ : while the vanadium atoms do not generate magnetic moments, the strong spin Berry curvature associated with the kagome Dirac cones leads to a significantly enhanced orbital Zeeman effect [20]. The high-spin Tb moments ( $J = 6$ ) order ferromagnetically below  $T_C = 4.4$  K and have strong Ising anisotropy based on heat capacity and low-field magnetization data [21, 22]. Magnetic heat capacity data are consistent with an isolated crystal electric field (CEF) doublet ground state [23], suggesting that this material may be a good candidate for investigating transverse-field Ising quantum criticality and its interaction with conduction electrons.

In the transverse-field Ising model (TFIM) [24], a transverse magnetic field leads to a quantum critical point (QCP) between Ising ferromagnetism and quantum paramagnetism. Strong quantum fluctuations near a QCP lead to highly non-classical behavior and exotic phases of matter [25]. There are only a few quantum ferromagnetic materials, like  $\text{LiHoF}_4$  [26], that are described by an effective spin-1/2 TFIM up to the critical transverse field, and weakly correlated metallic versions have not been studied.

It is an open question whether  $\text{TbV}_6\text{Sn}_6$  will exhibit features of TFIM quantum criticality. Even if the transition remains second order, the coupling of the Tb moments to the transverse spin fluctuations of conduction electrons will eventually drive the transition first order [27, 28], as seen in heavy fermion materials like  $\text{UGe}_2$  [29] and  $\text{URhGe}$  [30]. However, the expected effect here is much weaker and may allow the quantum critical behavior to be observed at finite temperatures; in what follows, we consider the intrinsic quantum crit-

ical behavior in the absence of conduction electrons. An alternate outcome is that the effect of a transverse field on the excited CEF states may lead to a breakdown of the isolated Ising doublet and thus a first-order metamagnetic transition [31].

In this Letter, we investigate the Ising nature of  $\text{TbV}_6\text{Sn}_6$  using inelastic neutron scattering (INS) and high-field magnetization measurements. The INS data allows us to determine the CEF parameters, which characterize a magnetic Hamiltonian with an isolated non-Kramers quasi-doublet (Ising) ground state at zero field. To search for evidence of TFIM quantum criticality, we measure the magnetization in transverse field and observe a first-order-like metamagnetic (spin-reorientation) transition near 25.6 T. This transition should exhibit a tricritical wing structure [32] with quantum critical endpoints occurring in small longitudinal fields. Analysis of our magnetic Hamiltonian indicates that the development of TFIM quantum criticality in  $\text{TbV}_6\text{Sn}_6$  is indeed preempted by a CEF level crossing near 26 T, in agreement with the magnetization data. However, this level crossing can be avoided with a slightly larger planar CEF anisotropy.  $\text{TbV}_6\text{Sn}_6$  is therefore proximate to a novel realization of a quantum tricritical point tuned by in-plane magnetic anisotropy.

*Neutron scattering data.* INS measurements on a polycrystalline sample of  $\text{TbV}_6\text{Sn}_6$  were performed on the Cold Neutron Chopper Spectrometer (CNCS) at the Spallation Neutron Source at Oak Ridge National Laboratory using incident neutron energies of  $E_i = 3.32$  meV and 12 meV. The measured INS intensity is proportional to the spin-spin correlation function  $\mathcal{S}(Q, \omega)$  where  $Q$  is the momentum transfer, and  $\omega = \Delta E/\hbar$  is the energy transfer. The data is histogrammed with bin sizes of  $\delta E = 0.06$  meV and  $\delta Q = 0.02 \text{ \AA}^{-1}$  using *DAVE* software [34].

Figures 1(c) and (d) show the INS data at  $T = 30$  K, well above  $T_C = 4.4$  K, with  $E_i = 12$  meV and  $E_i = 3.32$  meV respectively. These data show multiple non-dispersive excitations between the  $\text{Tb}^{3+}$  ion CEF levels. The  $Q$ -averaged intensities [within the red boxes in Figs. 1(c) and (d)] for dif-

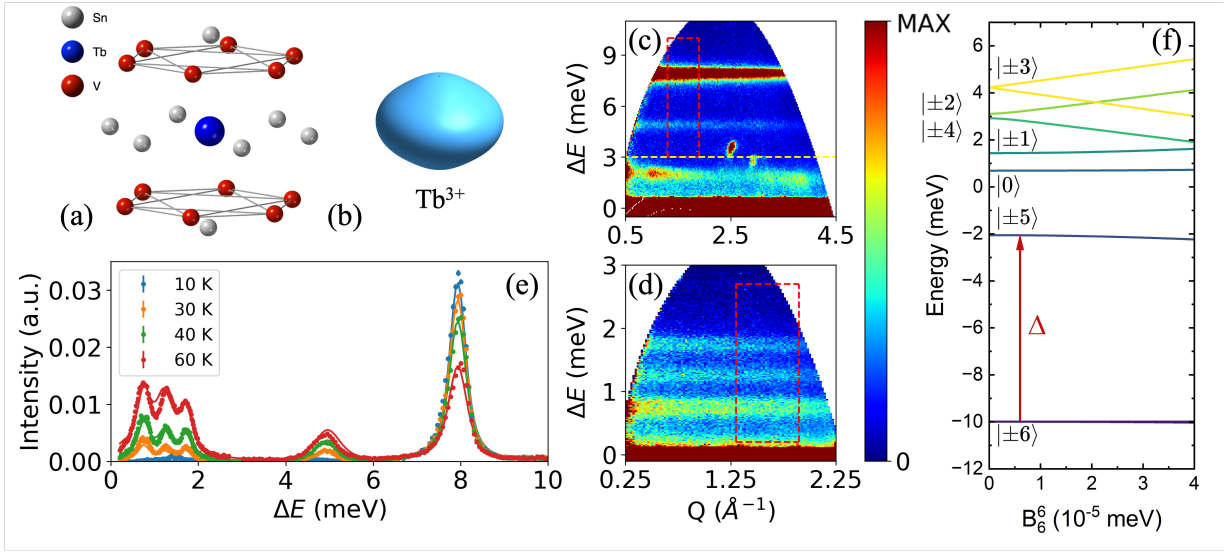


FIG. 1. **Crystal-field excitations of TbV<sub>6</sub>Sn<sub>6</sub>.** (a) The  $D_{6h}$  point-group symmetry environment centered at Tb<sup>3+</sup> ion, and the oblate-shaped Tb-4f charge density of the Tb<sup>3+</sup> ion in (b) indicates the strong anisotropy along the  $c$ -axis. The INS data with incident neutron energy of (c)  $E_i = 12$  meV and (d)  $E_i = 3.32$  meV showing CEF transitions at  $T = 30$  K. Data near and below the yellow dashed line in (c) are corrupted by spurious instrumental background. (e) The energy-dependence of the combined  $E_i = 3.32$  and 12 meV INS spectra showing CEF transition intensities at various temperatures (dots). Intensities at each  $E_i$  and  $T$  are averaged over the same  $Q$  range indicated by the dashed red boxes in (c) and (d) and have a fitted background removed. Data for different  $E_i$  are placed on the same intensity scale using procedures described in the SI [33]. Fits to the INS spectra from CEF calculations are plotted as solid lines in (e). (f) Zero-field CEF energy levels are obtained by varying  $B_6^6$  while keeping other CEF parameters fixed. CEF states have pure  $|\pm m_j\rangle$  eigenstates when  $B_6^6 = 0$ .

ferent  $E_i$  are placed on the same intensity scale [see Supplementary Information (SI) [33]] and plotted versus energy in Fig. 1(e) for  $T = 10, 30, 40, 60$  K. The main transition out of the ground state appears at  $\Delta E = 7.9$  meV at  $T = 10$  K and its intensity drops as the ground state thermally depopulates when raising the temperature. Multiple transitions occur nearly concurrently above 30 K suggesting that excited CEF levels are well-separated from the ground state doublet, but lie close to each other in energy.

Detailed information about the CEF can be obtained by fitting the INS spectra. The Hamiltonian for a Tb<sup>3+</sup> ion in a hexagonal CEF with  $D_{6h}$  point-group symmetry [see Fig. 1(a)] is

$$\mathcal{H}_{\text{CEF}} = B_2^0 \mathcal{O}_2^0 + B_4^0 \mathcal{O}_4^0 + B_6^0 \mathcal{O}_6^0 + B_6^6 \mathcal{O}_6^6. \quad (1)$$

We assume the Tb ion is in its Hund's rule ground state with total angular momentum  $J = 6$  ( $S = 3$ ,  $L = 3$ , and  $g_J = 3/2$ ).  $\mathcal{O}_l^m$  are the corresponding Steven's operator equivalents for  $J = 6$  and  $B_l^m$  are the CEF parameters.

For measurement of CEF excitations in powder samples with unpolarized neutrons, the neutron intensity is given by

$$\mathcal{S}(Q, \omega) \propto \sum_{m,n} \sum_{\alpha} p_m |\langle \Gamma_n | J_{\alpha} | \Gamma_m \rangle|^2 \delta(E_n - E_m - \hbar\omega). \quad (2)$$

Here,  $m$  labels an initial CEF state  $|\Gamma_m\rangle$  with energy  $E_m$  and thermal population  $p_m$  and  $n$  labels a final state  $|\Gamma_n\rangle$  with energy  $E_n$ . INS transitions follow the dipole selection rules

for  $J_{\alpha=x,y,z}$  matrix elements ( $\Delta m_j = 0, \pm 1$ , where  $m_j$  is the magnetic quantum number).

Using both the *PyCrystalField* and *LMFIT* package [35, 36], we simultaneously fit INS spectra at all temperatures in Fig. 1(e) using Eqns. (1) and (2). We use the Voigt peak profile convoluting the resolution and intrinsic widths since the CEF peaks are broader than the instrumental resolution. The best fit with  $\chi^2_{\nu} = 8.56$  is shown as lines in Fig. 1(e) and finds the following CEF parameters:  $B_2^0 = -0.1036(4)$ ,  $B_4^0 = -5.91(2) \times 10^{-4}$ ,  $B_6^0 = 2.31(2) \times 10^{-6}$ , and  $B_6^6 = 3.3(6) \times 10^{-6}$  meV. Given the relatively small value of  $B_6^6$ , the CEF eigenstates can be labeled by  $|\Gamma_m\rangle \approx |m_j\rangle$  with the  $\mathcal{O}_6^6$  operator causing small mixing between  $|m_j\rangle$  and  $|m_j \pm 6\rangle$  states (the eigenvectors are listed SI Table S1 [33]).

Figure 1(f) shows the calculated CEF levels for different values of  $B_6^6$ . As expected, we find that the ground state is an Ising doublet  $|\pm 6\rangle$  with a strongly anisotropic orbital wave function shown in Fig. 1(b). The ground state doublet is well separated from the first excited state  $|\pm 5\rangle$  by  $\Delta = 7.9$  meV. The ratio  $k_B T_C / \Delta \approx 0.05$  is a signature of the Ising character of the FM ordered state. These CEF parameters are consistent with the expectations for an Ising magnet and thermodynamic calculations from our CEF model agree with magnetization (see below), susceptibility, and heat capacity data (see Fig. S1 in the SI [33]).

*High-field magnetization data.* To search for evidence of TFIM quantum criticality, we performed magnetization measurements on TbV<sub>6</sub>Sn<sub>6</sub> in pulsed magnetic fields up to 60 T at National High Magnetic Field Laboratory in Los Alamos.

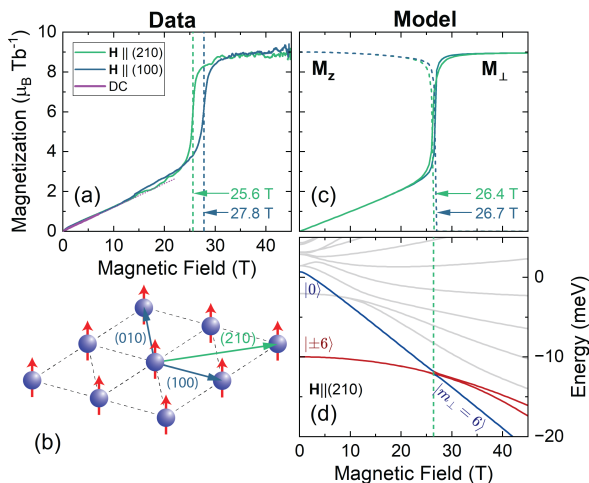


FIG. 2. **Transverse-field magnetization of  $\text{TbV}_6\text{Sn}_6$ .** (a) Transverse pulsed-field magnetization data measured for fields along (100) and (210) directions at  $T = 625$  mK. Low-field DC data measured at 1.8 K are shown for comparison. (b) Triangular Tb layer showing field directions. (c) Mean-field model calculations of the magnetization components parallel to the (100) and (210) applied field directions ( $M_\perp$ , solid lines) and perpendicular to the applied field along (001) ( $M_z$ , dashed lines). (d) Evolution of crystal-field levels as a function of transverse field applied along (210). The Ising state doublet (red lines) and the state that evolves from the zero-field  $|m_j = 0\rangle$  state to the planar  $|m_\perp = 6\rangle$  state (blue line) are highlighted.

Two different crystal mountings were investigated with the field parallel to inequivalent (100) or (210) high-symmetry directions in the hexagonal plane, as shown in Fig. 2(b). Fig. 2(a) compares the magnetization with field applied in either direction (raw  $dM/dH$  data and fits are shown SI Fig. S3 [33]). The magnetization initially tilts weakly towards the field due to the strong Ising anisotropy and then jumps parallel to the field in a first-order-like spin-reorientation transition. We observe critical fields of 25.6 T and 27.8 T for (210) and (100) field directions, respectively. The first-order-like character of the spin-reorientation transition suggests that true TFIM quantum criticality, typified by a second-order transition as  $T \rightarrow 0$ , is not achieved in  $\text{TbV}_6\text{Sn}_6$ .

Independent estimates of the  $B_l^0$  CEF parameters derived from magnetization data are described in the SI [33] and provide values similar to INS data. The observed critical field anisotropy of 2.2 T between the two field directions should, in principle, also allow for an independent determination of the planar CEF anisotropy  $B_6^6$  with an easy axis along the (210) direction ( $B_6^6 > 0$ ).

To study the planar anisotropy in more detail, high-field proximity detector oscillator (PDO) measurements described in the SI [33] were performed as a function of the in-plane field direction. PDO measurements find a minimum critical field of 25.6 T for  $\mathbf{H} \parallel (210)$ , but also find a prominent two-fold rotational component, rather than six-fold, that suggests sample misalignment. Misalignment is caused by strong sample torque that tilts the crystal and introduces a

small component of the applied field along the (001) axis. Tilting increases the apparent critical field by approximately one Tesla per degree of tilt (see SI [33]). Thus, the observed critical field anisotropy can only set an upper limit for  $B_6^6 \lesssim 30 \times 10^{-6}$  meV, which is much greater than the  $B_6^6$  value determined from the best fit to INS data.

*Theoretical analysis.* To understand the apparent first-order nature of the spin-reorientation transition and avoided quantum criticality, we extend the CEF Hamiltonian in Eqn. (1) to include the applied transverse field and an effective isotropic ferromagnetic Heisenberg coupling between Tb moments,

$$\mathcal{H} = \mathcal{H}_{\text{CEF}} - \frac{1}{2} \sum_{ij} \mathcal{J}_{ij} \vec{J}_i \cdot \vec{J}_j - g_L \mu_B \vec{B} \cdot \sum_i \vec{J}_i, \quad (3)$$

where  $\vec{J}$  is the Tb moment. Hyperfine corrections to the phase diagram and long-range dipolar interactions are estimated to be small, as discussed in the SI [33]. We use a mean-field (MF) approximation to self-consistently solve for  $\langle \vec{J} \rangle$  at different fields and temperatures. The MF transition temperature is set by  $\mathcal{J}_0 = \sum_j \mathcal{J}_{ij}$  and we choose  $\mathcal{J}_0 = 122$  mK to reproduce the experimental  $T_C = 4.4$  K. Fluctuations will decrease the critical temperature, making this value a lower bound of the interaction strength.

Using the INS-derived CEF parameters, MF calculations find a first-order spin-reorientation transition for all in-plane field directions. The calculated magnetization,  $\vec{M} = g_J \langle \vec{J} \rangle$  as a function of transverse field is shown in Fig. 2(c), where the critical fields are weakly anisotropic: 26.4 T along the (210) easy-axis and 26.7 T along (100). These critical fields agree with the high-field magnetization within 1 T, but the apparent anisotropy seen in Fig. 2(a) is not reproduced unless sample tilt is accounted for (see Fig. S7 of the SI [33]).

Figure 2(d) shows that the spin-reorientation transition is caused by a CEF level crossing in the transverse field, rather than a TFIM QCP. The transition is first-order because the  $|\pm 6\rangle$  levels, shown in red, have barely begun to split before being crossed by the original  $|0\rangle$  level. The effective transverse field for the ground state doublet is therefore still relatively far from the TFIM QCP when the level crossing occurs. Above the critical field, the ground state is  $\approx |m_\perp = 6\rangle$ , appropriate for a field-aligned planar moment.

At elevated temperatures and low fields, MF calculations indicate that the transition becomes second order, with tricritical points at  $T_{tcp} = 1.65$  K and 1 K along the (100) and (210) axis, respectively. These tricritical points lead to a compact wing structure [32] in longitudinal fields, with quantum critical end points (QCEPs) expected at  $(B_x, B_z) \approx (27, \pm 0.2)$  T. It is unclear whether these QCEPs lead to observable consequences, as sample alignment difficulties make observing the wing structure difficult.

*Quantum criticality.* Based on this examination of a single set of experimentally derived CEF parameters, we might conclude that  $\text{TbV}_6\text{Sn}_6$  is a poor candidate for TFIM quantum criticality. However, the nature of the criticality is highly sensitive to the CEF parameters, particularly the  $B_6^6$  parameter

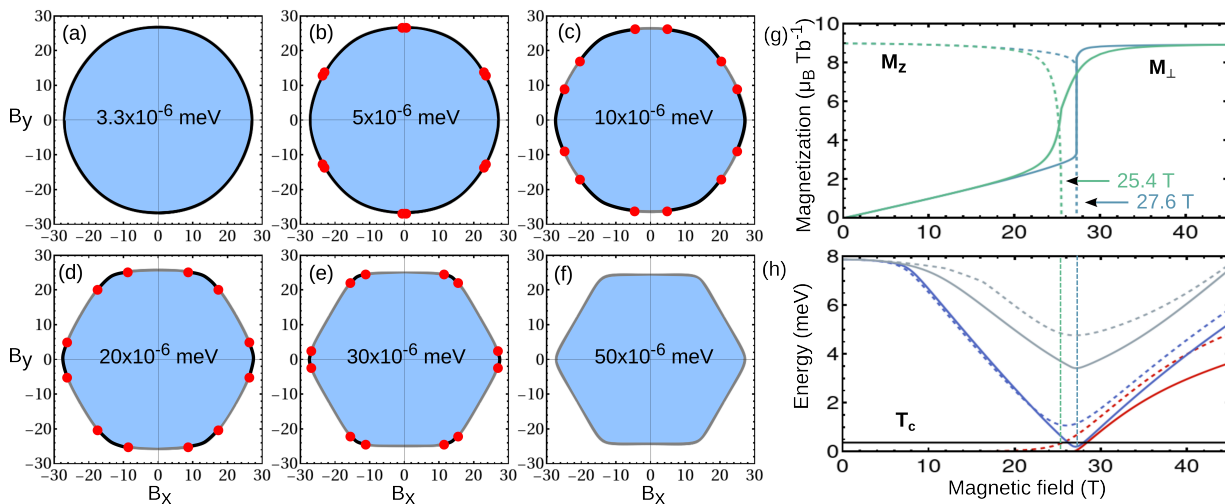


FIG. 3. **Development of quantum tricritical behavior.** (a)-(f) The  $T = 0$  phase diagram as a function of transverse field in the  $B_x - B_y$  plane for several  $B_6^6$  values with all other CEF parameters and  $\mathcal{J}_0$  held fixed. The blue regions are ferromagnetic and the white regions are quantum paramagnetic. There are two critical  $B_6^6$ 's: a lower  $B_6^6 = 4.6 \times 10^{-6}$  meV, below which all transitions are first order (black), and an upper  $B_6^6 = 33 \times 10^{-6}$  meV, above which all transitions are second order (gray). In-between, there are QTCPs at certain angles (red dots) that separate the first and second-order lines. The fitted CEF parameters with  $B_6^6 = 3.3 \times 10^{-6}$  meV give the phase diagram in (a). (g),(h) We fix  $B_6^6 = 20 \times 10^{-6}$  meV, and show (g) the magnetization for fields parallel to the (100) (blue lines) and (210) direction (green lines). Comparing to Fig. 2(c), the transition along (210) has become second order and the critical-field anisotropy has increased significantly. Panel (h) shows the evolution of the crystal-field levels along  $\mathbf{H} \parallel (100)$  (solid lines) and  $\mathbf{H} \parallel (210)$  (dashed lines), now adjusted such that the ground state is always at 0 meV. The first excited state, which corresponds to the upper level of the Ising doublet at low fields is highlighted in red, while the second excited state is in blue. The solid black horizontal line shows  $k_B T_C = 0.38$  meV. For  $\mathbf{H} \parallel (100)$ , the first-order transition occurs at the minimum of the splitting to the second excited state, while for  $\mathbf{H} \parallel (210)$ , the second-order transition occurs where the first excited state is at approximately  $k_B T_C$ ; these critical fields are indicated by the dashed lines.

governing the in-plane magnetic anisotropy.

In fact,  $\text{TbV}_6\text{Sn}_6$  appears to be remarkably close to a novel type of quantum tricriticality favored by intermediate strength of the in-plane magnetic anisotropy. To illustrate this, we study how the quantum criticality is tuned by  $B_6^6$  with other parameters held fixed. The ground state phase diagrams in transverse fields are shown in Fig. 3(a)-(f) for several values of  $B_6^6$ , where there are clearly two critical values of  $B_6^6$ . Below the lower critical  $B_6^6 = 4.6 \times 10^{-6}$  meV, the transitions are all first order, as discussed above, but above it, a line of second order transitions nucleates around the (210) easy axis, separated from the first order transitions by quantum tricritical points (QTCPs) at finite field angles. As  $B_6^6$  increases, the line of second order QCPs grow until the QTCPs disappear at the upper critical  $B_6^6 = 33 \times 10^{-6}$  meV and the transition is second order for all in-plane field directions. The in-plane magnetic anisotropy grows noticeably, with the phase diagram appearing nearly circular for small  $B_6^6$  and hexagonal near the upper critical  $B_6^6$ .

In Fig. 3(g), we show a plot of the magnetization versus in-plane field for  $B_6^6 = 20 \times 10^{-6}$  meV, with the corresponding CEF levels shown in Fig. 3(h). The TFIM criticality occurs when  $k_B T_C$  is approximately equal to the splitting of the Ising doublet, but it can be preempted if  $k_B T_C$  is on the order of the CEF excited state energy. The second-order transition along the easy (210) axis is driven by the  $B_6^6$  mixing that causes a repulsion between the Ising doublet and the excited CEF

state. Level mixing lowers the critical field and preserves the second-order nature. Along the hard (100) axis, the first-order transition occurs roughly when the minimum of the excited CEF level is on the order of  $k_B T_C$ . The critical  $B_6^6$  values thus depend sensitively on  $k_B T_C$ , with the lower critical  $B_6^6$  increased by a factor of five when  $k_B T_C$  doubles.

*Discussion.* We have shown that the kagome metal  $\text{TbV}_6\text{Sn}_6$  is a good realization of an Ising magnet. Remarkably, whether or not it exhibits a TFIM quantum phase transition depends sensitively on the crystal fields and the angle of the transverse field in the  $ab$ -plane. This discovery reveals a rare opportunity to address the nature and tunability of quantum critical Ising behavior in a non-heavy-fermion metal.

Our measurements suggest that the standard TFIM quantum criticality is likely avoided, but the true nature of quantum criticality in  $\text{TbV}_6\text{Sn}_6$  has proven to be somewhat unresolved and elusive.  $\text{TbV}_6\text{Sn}_6$  is likely quite close to a lower critical  $B_6^6 = 4.6 \times 10^{-6}$  meV, above which the quantum critical nature varies with the field angle, including QTCPs at particular angles. While the INS determined value,  $B_6^6 = 3.3 \times 10^{-6}$  meV is below this threshold, the threshold is well within the upper limit determined by the critical field anisotropy ( $< 30 \times 10^{-6}$  meV) and density-functional theory estimates ( $21 \times 10^{-6}$  meV, see SI [33]). We note that larger values of  $B_6^6$  will not affect the Ising character of  $\text{TbV}_6\text{Sn}_6$ , as shown in Fig. 1(f). However, mixing will increase the number of dipole-allowed CEF transitions observed below 2 meV in INS.

Accounting for these extra transitions in our fitting [Fig. 1(e)] is difficult given the broad lineshape of the excitations and it is possible that  $B_6^6$  is underestimated in our INS fits (see SI Fig. S2 [33] for more details). Furthermore, while theoretical analysis can resolve a weakly first-order transition from a second-order transition, experimental determination of the order of the phase transition on real materials can be ambiguous.

Thus, our analysis places  $\text{TbV}_6\text{Sn}_6$  within the reach of novel, field-angle-tuned quantum critical and tricritical behavior. Tricritical points separate first and second-order critical lines; quantum tricritical points are simply when these occur at  $T = 0$ , and can be modeled with  $\phi^6$  Landau theories involving one or more order parameters. Proximity to quantum tricritical points has been suggested to explain unusual behavior in  $\text{Sr}_3\text{Ru}_2\text{O}_7$  [37–39],  $\text{URhGe}$  [40, 41],  $\text{YbRh}_2\text{Si}_2$  and other materials [42–46].

The fields required to tune  $\text{TbV}_6\text{Sn}_6$  to the vicinity of its critical fields are large, but experimentally accessible, making it a potential testing ground to compare the signatures of quantum criticality and quantum tricriticality just by tuning the angle of the in-plane magnetic field. One interesting possibility is to search for the finite temperature signatures of quantum criticality, where the longitudinal magnetic susceptibility should diverge with different power laws above the QTCPs,  $\chi_{zz} \sim T^{-2\psi}$ , compared to the QCPs,  $\chi_{zz} \sim T^{-\psi}$  [39, 47], where  $\psi$  is likely two for short range three-dimensional interactions. However, sample misalignment in the presence of large torques would need to be very carefully avoided, as a finite longitudinal field component will cut off this critical behavior. Alternately, the critical points may be masked by the formation of new low temperature phases, as with the superconductivity in  $\text{URhGe}$  [40, 41] and the nematic spin density waves in ultrapure  $\text{Sr}_3\text{Ru}_2\text{O}_7$  [38, 48]. It is also desirable to tune  $RT_6X_6$  materials (by chemical substitution, for example) to increase the planar anisotropy to provide a more definitive example of quantum tricriticality.

*Acknowledgments.* TH, RDM, YL, BL, LK, RF, and RJM’s work at the Ames National Laboratory is supported by the U.S. Department of Energy, Office of Science, Basic Energy Sciences, Materials Science and Engineering. JB, TJS, PCC, RM’s work was supported by the Center for the Advancement of Topological Semimetals (CATS), an Energy Frontier Research Center funded by the U.S. Department of Energy (DOE) Office of Science (SC), Office of Basic Energy Sciences (BES), through the Ames National Laboratory. Ames National Laboratory is operated for the USDOE by Iowa State University under Contract No. DE-AC02-07CH11358. This research used resources at the Spallation Neutron Source, a DOE Office of Science User Facility operated by the Oak Ridge National Laboratory. A portion of this work was performed at the National High Magnetic Field Laboratory, which is supported by National Science Foundation Cooperative Agreement No. DMR-2128556, the U.S. Department of Energy (DoE), and the state of Florida.

- [1] Y.-X. Jiang, J.-X. Yin, M. M. Denner, N. Shumiya, B. R. Ortiz, G. Xu, Z. Guguchia, J. He, M. S. Hossain, X. Liu, J. Ruff, L. Kautzsch, S. S. Zhang, G. Chang, I. Belopolski, Q. Zhang, T. A. Cochran, D. Multer, M. Litskevich, Z.-J. Cheng, X. P. Yang, Z. Wang, R. Thomale, T. Neupert, S. D. Wilson, and M. Z. Hasan, Unconventional chiral charge order in kagome superconductor  $\text{KV}_3\text{Sb}_5$ , *Nat. Mater.* **20**, 1353 (2021).
- [2] X. Teng, L. Chen, F. Ye, E. Rosenberg, Z. Liu, J.-X. Yin, Y.-X. Jiang, J. S. Oh, M. Z. Hasan, K. J. Neubauer, B. Gao, Y. Xie, M. Hashimoto, D. Lu, C. Jozwiak, A. Bostwick, E. Rotenberg, R. J. Birgeneau, J.-H. Chu, M. Yi, and P. Dai, Discovery of charge density wave in a kagome lattice antiferromagnet, *Nature* **609**, 490 (2022).
- [3] H. W. S. Arachchige, W. R. Meier, M. Marshall, T. Matsuoaka, R. Xue, M. A. McGuire, R. P. Hermann, H. Cao, and D. Mandrus, Charge Density Wave in Kagome Lattice Intermetallic  $\text{ScV}_6\text{Sn}_6$ , *Phys. Rev. Lett.* **129**, 216402 (2022).
- [4] H. Tan, Y. Liu, Z. Wang, and B. Yan, Charge Density Waves and Electronic Properties of Superconducting Kagome Metals, *Phys. Rev. Lett.* **127**, 046401 (2021).
- [5] B. R. Ortiz, P. M. Sarte, E. M. Kenney, M. J. Graf, S. M. L. Teicher, R. Seshadri, and S. D. Wilson, Superconductivity in the  $\mathbb{Z}_2$  kagome metal  $\text{KV}_3\text{Sb}_5$ , *Phys. Rev. Mater.* **5**, 034801 (2021).
- [6] B. R. Ortiz, L. C. Gomes, J. R. Morey, M. Winiarski, M. Bordelon, J. S. Mangum, I. W. H. Oswald, J. A. Rodriguez-Rivera, J. R. Neilson, S. D. Wilson, E. Ertekin, T. M. McQueen, and E. S. Toberer, New kagome prototype materials: discovery of  $\text{KV}_3\text{Sb}_5$ ,  $\text{RbV}_3\text{Sb}_5$ , and  $\text{CsV}_3\text{Sb}_5$ , *Phys. Rev. Mater.* **3**, 094407 (2019).
- [7] S.-Y. Yang, Y. Wang, B. R. Ortiz, D. Liu, J. Gayles, E. Derunova, R. Gonzalez-Hernandez, L. Šmejkal, Y. Chen, S. S. P. Parkin, S. D. Wilson, E. S. Toberer, T. McQueen, and M. N. Ali, Giant, unconventional anomalous Hall effect in the metallic frustrated magnet candidate,  $\text{KV}_3\text{Sb}_5$ , *Sci. Adv.* **6**, eabb6003 (2020).
- [8] J. Cable, N. Wakabayashi, and P. Radhakrishna, A neutron study of the magnetic structure of  $\text{Mn}_3\text{Sn}$ , *Solid State Communications* **88**, 161 (1993).
- [9] N. J. Ghimire, R. L. Dally, L. Poudel, D. C. Jones, D. Michel, N. T. Magar, M. Bleuel, M. A. McGuire, J. S. Jiang, J. F. Mitchell, J. W. Lynn, and I. I. Mazin, Competing magnetic phases and fluctuation-driven scalar spin chirality in the kagome metal  $\text{YMn}_6\text{Sn}_6$ , *Sci. Adv.* **6**, eabe2680 (2020).
- [10] R. L. Dally, J. W. Lynn, N. J. Ghimire, D. Michel, P. Siegfried, and I. I. Mazin, Chiral properties of the zero-field spiral state and field-induced magnetic phases of the itinerant kagome metal  $\text{YMn}_6\text{Sn}_6$ , *Phys. Rev. B* **103**, 094413 (2021).
- [11] Y.-F. Zhang, X.-S. Ni, T. Datta, M. Wang, D.-X. Yao, and K. Cao, Ab initio study of spin fluctuations in the itinerant kagome magnet  $\text{FeSn}$ , *Phys. Rev. B* **106**, 184422 (2022).
- [12] Y. Lee, R. Skomski, X. Wang, P. P. Orth, Y. Ren, B. Kang, A. K. Pathak, A. Kutepov, B. N. Harmon, R. J. McQueeney, I. I. Mazin, and L. Ke, Interplay between magnetism and band topology in the kagome magnets  $\text{RMn}_6\text{Sn}_6$ , *Phys. Rev. B* **108**, 045132 (2023).
- [13] J.-X. Yin, W. Ma, T. A. Cochran, X. Xu, S. S. Zhang, H.-J. Tien, N. Shumiya, G. Cheng, K. Jiang, B. Lian, Z. Song, G. Chang, I. Belopolski, D. Multer, M. Litskevich, Z.-J. Cheng, X. P. Yang, B. Swidler, H. Zhou, H. Lin, T. Neupert, Z. Wang, N. Yao, T.-R. Chang, S. Jia, and M. Zahid Hasan, Quantum-

- limit Chern topological magnetism in  $\text{TbMn}_6\text{Sn}_6$ , *Nature* **583**, 533 (2020).
- [14] S. Baidya, S. Kang, C. H. Kim, and J. Yu, Chern insulator with a nearly flat band in the metal-organic-framework-based Kagome lattice, *Scientific Reports* **9**, 13807 (2019).
- [15] Y. Ren, H.-C. Jiang, Z. Qiao, and D. N. Sheng, Orbital Chern Insulator and Quantum Phase Diagram of a Kagome Electron System with Half-Filled Flat Bands, *Phys. Rev. Lett.* **126**, 117602 (2021).
- [16] H.-M. Guo and M. Franz, Topological insulator on the kagome lattice, *Phys. Rev. B* **80**, 113102 (2009).
- [17] B. Chafik El Idrissi, G. Venturini, and B. Malaman, Refinement of  $\text{HfFe}_6\text{Ge}_6$  isostructural  $\text{ScMn}_6\text{Sn}_6$  and  $\text{TbMn}_6\text{Sn}_6$ , *Materials Research Bulletin* **26**, 431 (1991).
- [18] L. Romaka, Y. Stadnyk, V. Romaka, P. Demchenko, M. Stannyshyn, and M. Konyk, Peculiarities of component interaction in  $\{\text{Gd}, \text{Er}\}-\text{V}-\text{Sn}$  Ternary systems at 870K and crystal structure of  $\text{RV}_6\text{Sn}_6$  stannides, *Journal of Alloys and Compounds* **509**, 8862 (2011).
- [19] G. Venturini, R. Welter, and B. Malaman, Crystallographic data and magnetic properties of  $\text{RT}_6\text{Ge}_6$  compounds ( $R \equiv \text{Sc}, \text{Y}, \text{Nd}, \text{Sm}, \text{Gd}-\text{Lu}; T \equiv \text{Mn}, \text{Fe}$ ), *Journal of Alloys and Compounds* **185**, 99 (1992).
- [20] Y. Hu, X. Wu, Y. Yang, S. Gao, N. C. Plumb, A. P. Schnyder, W. Xie, J. Ma, and M. Shi, Tunable topological dirac surface states and van hove singularities in kagome metal  $\text{gdv}_1\text{sub}_\zeta 6_1/\text{sub}_\zeta \text{sn}_1\text{sub}_\zeta 6_1/\text{sub}_\zeta$ , *Science Advances* **8**, eadd2024 (2022), <https://www.science.org/doi/pdf/10.1126/sciadv.add2024>.
- [21] E. Rosenberg, J. M. DeStefano, Y. Guo, J. S. Oh, M. Hashimoto, D. Lu, R. J. Birgeneau, Y. Lee, L. Ke, M. Yi, and J.-H. Chu, Uniaxial ferromagnetism in the kagome metal  $\text{TbV}_6\text{Sn}_6$ , *Phys. Rev. B* **106**, 115139 (2022).
- [22] X. Zhang, Z. Liu, Q. Cui, Q. Guo, N. Wang, L. Shi, H. Zhang, W. Wang, X. Dong, J. Sun, Z. Dun, and J. Cheng, Electronic and magnetic properties of intermetallic kagome magnets  $\text{RV}_6\text{Sn}_6$  ( $R = \text{Tb}-\text{Tm}$ ), *Phys. Rev. Mater.* **6**, 105001 (2022).
- [23] G. Pokharel, B. Ortiz, J. Chamorro, P. Sarte, L. Kautzsch, G. Wu, J. Ruff, and S. D. Wilson, Highly anisotropic magnetism in the vanadium-based kagome metal  $\text{TbV}_6\text{Sn}_6$ , *Phys. Rev. Mater.* **6**, 104202 (2022).
- [24] P. G. de Gennes, Collective Motions of Hydrogen Bonds, *Solid State Communications* **1**, 132 (1963).
- [25] S. Sachdev, *Quantum Phase Transitions*, 1st ed. (Cambridge University Press, 1999).
- [26] D. Bitko, T. F. Rosenbaum, and G. Aeppli, Quantum Critical Behavior for a Model Magnet, *Phys. Rev. Lett.* **77**, 940 (1996).
- [27] D. Belitz, T. R. Kirkpatrick, and T. Vojta, First order transitions and multicritical points in weak itinerant ferromagnets, *Phys. Rev. Lett.* **82**, 4707 (1999).
- [28] T. R. Kirkpatrick and D. Belitz, Universal low-temperature tricritical point in metallic ferromagnets and ferrimagnets, *Phys. Rev. B* **85**, 134451 (2012).
- [29] V. Taufour, D. Aoki, G. Knebel, and J. Flouquet, Tricritical point and wing structure in the itinerant ferromagnet  $\text{Uge}_2$ , *Phys. Rev. Lett.* **105**, 217201 (2010).
- [30] E. A. Yelland, J. M. Barraclough, W. Wang, K. V. Kamenev, and A. D. Huxley, High-field superconductivity at an electronic topological transition in  $\text{Urhge}$ , *Nature Physics* **7**, 890 (2011).
- [31] P. Stasiak and M. J. P. Gingras, Assessment of the  $\text{RE}(\text{OH})_3$  Ising magnetic materials as possible candidates for the study of transverse-field-induced quantum phase transitions, *Phys. Rev. B* **78**, 224412 (2008).
- [32] R. B. Griffiths, Thermodynamics Near the Two-Fluid Critical Mixing Point in  $\text{He}^3\text{-He}^4$ , *Phys. Rev. Lett.* **24**, 715 (1970).
- [33] See Supplementary Information, doi:xxxx.
- [34] R. T. Aзуаh, L. R. Kneller, Y. Qiu, P. L. W. Tregenna-Piggott, C. M. Brown, J. R. D. Copley, and R. M. Dimeo, DAVE: A comprehensive software suite for the reduction, visualization, and analysis of low energy neutron spectroscopic data, *J Res Natl Inst Stand Technol* **114**, 341 (2009).
- [35] A. Scheie, *PyCrystalField*: software for calculation, analysis and fitting of crystal electric field Hamiltonians, *Journal of Applied Crystallography* **54**, 356 (2021).
- [36] M. Newville, T. Stensitzki, D. B. Allen, and A. Ingargiola, LM-FIT: Non-Linear Least-Square Minimization and Curve-Fitting for Python (2015).
- [37] S. A. Grigera, R. A. Borzi, A. P. Mackenzie, R. S. Perry, and Y. Maeno, Angular dependence of the magnetic susceptibility in the itinerant metamagnet  $\text{Sr}_3\text{Ru}_2\text{O}_7$ , *Phys. Rev. B* **67**, 214427 (2003).
- [38] A. G. Green, S. A. Grigera, R. A. Borzi, A. P. Mackenzie, R. S. Perry, and B. D. Simons, Phase Bifurcation and Quantum Fluctuations in  $\text{Sr}_3\text{Ru}_2\text{O}_7$ , *Phys. Rev. Lett* **95**, 086402 (2005).
- [39] M. T. Mercaldo, I. Rabuffo, A. Naddeo, A. C. D'Auria, and L. D. Cesare, Quantum tricriticality in transverse Ising-like systems, *Eur. Phys. J. B* **84**, 371 (2011).
- [40] F. Lévy, I. Sheiken, B. Grenier, and A. D. Huxley, Magnetic Field-Induced Superconductivity in the Ferromagnet  $\text{URhGe}$ , *Science* **309**, 1343 (2005).
- [41] A. D. Huxley, S. J. C. Yates, F. Lévy, and I. Sheiken, Odd-Parity Superconductivity and the Ferromagnetic Quantum Critical Point, *J. Phys. Soc. Jpn.* **76**, 051011 (2007).
- [42] T. Misawa, Y. Yamaji, and M. Imada,  $\text{YbRh}_2\text{Si}_2$ : Quantum tricritical behavior in itinerant electron systems, *Journal of the Physical Society of Japan* **77**, 093712 (2008), <https://doi.org/10.1143/JPSJ.77.093712>.
- [43] G. Giovannetti, C. Ortix, M. Marsman, M. Capone, J. van den Brink, and J. Lorenzana, Proximity of iron pnictide superconductors to a quantum tricritical point, *Nature Communications* **1**, 62 (2011).
- [44] S. Friedemann, W. J. Duncan, M. Hirschberger, T. W. Bauer, R. Küchler, A. Neubauer, M. Brando, C. Pfleiderer, and F. M. Grosche, Quantum tricritical points in  $\text{nbfe}_2$ , *Nature Physics* **14**, 62 (2018).
- [45] U. S. Kaluarachchi, V. Taufour, S. L. Bud'ko, and P. C. Canfield, Quantum tricritical point in the temperature-pressure-magnetic field phase diagram of  $\text{CeTlGe}_3$ , *Phys. Rev. B* **97**, 045139 (2018).
- [46] R. R. Ullah, J. S. Harvey, H. Jin, Y. Wu, H. B. Cao, J. R. Badger, P. Klavins, and V. Taufour, Avoided quantum tricritical point and emergence of a canted magnetic phase in  $\text{LaCr}_{1-x}\text{Fe}_x\text{Sb}_3$ , *Phys. Rev. Lett.* **133**, 096701 (2024).
- [47] Y. Kato and T. Misawa, Quantum tricriticality in antiferromagnetic ising model with transverse field: A quantum monte carlo study, *Phys. Rev. B* **92**, 174419 (2015).
- [48] C. Lester, S. Ramos, R. S. Perry, T. P. Croft, R. I. Bewley, T. Guidi, P. Manuel, D. D. Khalyavin, E. M. Forgan, and S. M. Hayden, Field-tunable spin-density-wave phases in  $\text{Sr}_3\text{Ru}_2\text{O}_7$ , *Nature Materials* **14**, 373 (2015).

## Supplementary Information - Proximity to quantum criticality in the Ising ferromagnet $\text{TbV}_6\text{Sn}_6$

Tianxiong Han,<sup>1,2</sup> R. D. McKenzie,<sup>1,2</sup> Joanna Blawat,<sup>3</sup> Tyler J. Slade,<sup>1</sup> Y. Lee,<sup>1</sup> D. M. Pajerowski,<sup>4</sup> John Singleton,<sup>3</sup> Bing Li,<sup>4</sup> Paul Canfield,<sup>1,2</sup> Liqin Ke,<sup>1</sup> Ross McDonald,<sup>3</sup> Rebecca Flint,<sup>1,2</sup> and R. J. McQueeney<sup>1,2</sup>

<sup>1</sup>Ames National Laboratory, U.S. DOE, Iowa State University, Ames, Iowa 50011, USA

<sup>2</sup>Department of Physics and Astronomy, Iowa State University, Ames, Iowa 50011, USA

<sup>3</sup>National High Magnetic Field Laboratory, Los Alamos National Laboratory, Los Alamos, NM 87545

<sup>4</sup>Oak Ridge National Laboratory, Oak Ridge, TN, 37831, USA

(Dated: December 4, 2024)

### SAMPLE PREPARATION AND CHARACTERIZATION

Single crystals were grown from a Sn flux similar to the previously described process [S1, S2]. An obstacle to growing large  $\text{TbV}_6\text{Sn}_6$  crystals, suitable for inelastic neutron scattering, is the relatively poor solubility of V in Sn. We found that the typical reactions described in earlier reports normally yielded mixtures of small  $\text{TbV}_6\text{Sn}_6$  crystals alongside chunks of (likely undissolved) V. We empirically found that by using the two step process described below, larger crystals can be produced.

Elemental pieces of Tb (Ames Lab, 99.99%), V (Alpha-Aesar, 99.99 %) and Sn (Alpha-Aesar, 99.99%) were weighed in a 1:6:60 molar ratio and loaded into the growth side of a 5 ml alumina Canfield crucible set [S3]. The crucibles were sealed under vacuum in a fused silica ampule and heated in a box furnace to 1180 C. After holding at 1180 C for  $\approx 24$  h, the samples were removed from the furnace and the liquid decanted in a metal centrifuge, upon which the liquid phase is cleanly captured in the second crucible on the top side of the crucible set. This first step allows us to cleanly separate the liquid from any undissolved V. A second sequence is then carried out, with the captured decant used in the "growth" side of a new crucible set. The second crucible set was sealed under vacuum as before and warmed in a box furnace to 1195 C. After holding at 1195 C for 6 h, the furnace was cooled to 775 C, upon which the ampule was removed from the furnace and the excess liquid decanted. Once cool, the ampules and crucibles were opened to reveal relatively large (5-10 mg), single phase, crystals of  $\text{TbV}_6\text{Sn}_6$ .

Low field ( $H = 0-7$  T) magnetization measurements were performed in a Quantum Design Magnetic Property Measurement System (MPMS-classic) SQUID magnetometer operating in the DC measurement mode. For measurements with  $\mathbf{H} \parallel (100)$ , the sample was mounted between two straws. For measurements with  $\mathbf{H} \parallel c$ , the sample was glued to a Kel-F disc. In the latter case, a blank reference sequence over the same temperature and fields was measured on the bare disc and used for a background subtraction. The temperature dependent measurements were field cooled starting at 300 K, and the magnetization isotherms measured on decreasing field from 7 T. Transverse field data are shown in Fig. ??(a) in the main text. Fig. S1(a) shows measurements of the anisotropic magnetic susceptibility compared to MF calculations [calculations of the magnetic heat capacity and entropy are also shown

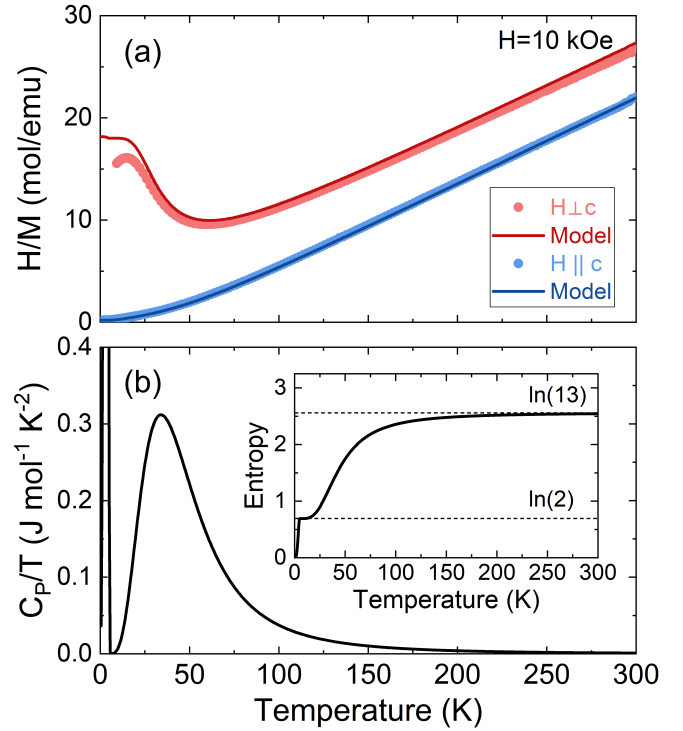


FIG. S1. (a) Transverse ( $H \perp c$ ) and longitudinal-field ( $H \parallel c$ ) magnetization data measured at 10 kOe (circles, plotted as the inverse susceptibility  $H/M$ ) versus temperature. Solid lines show predictions of the measurement from MF calculations. (b) MF calculations of the magnetic heat capacity versus temperature. Inset shows the magnetic entropy.

in Fig. S1(b)].

A polycrystalline sample for inelastic neutron scattering (INS) measurements was prepared by grinding the flux-grown single crystals using mortar and pestle, and sieving with a diameter of 32 micrometers to obtain particles of uniform size. A sample weighing 1.2 grams was sealed in the aluminum can filled with helium gas and mounted to a closed-cycle refrigerator for studies down to  $T = 1.7$  K.

## EXTENDED NEUTRON DATA ANALYSIS

### Eigenvalues and eigenvectors from CEF Hamiltonian

After diagonalizing the CEF Hamiltonian using the parameters in the main text, we obtain the zero-field the eigenvalues and eigenvectors, as shown in Table S1.

### CEF model with larger $B_6^6$ values

We investigated the possibility that larger  $B_6^6$  values can be used to fit the INS data. The reduced  $\chi_\nu^2$  map as a function of  $B_6^6$  and the intensity scaling ratio between  $E_i = 12$  and 3.3 meV data is shown in Fig. S2(a). Whereas the global minimum that provides best fit is reported in the main text (called Case I), another set of CEF parameters with much larger  $B_6^6$  (and larger scaling ratio) gives a local minimum (called Case II). Using the incoherent elastic line, we independently verified that the scaling ratio is in the range of 1 to 1.3 corresponding to the Case I global minimum.

The local minimum of Case II has CEF parameters with  $B_2^0 = -0.1151(3)$ ,  $B_4^0 = -5.57(1) \times 10^{-4}$ ,  $B_6^0 = 2.31(2) \times 10^{-6}$ ,  $2.30(5) \times 10^{-5}$  meV, and  $\chi_\nu^2 = 11.64$  for comparison. The calculated neutron spectrum from Case II parameters compared to the measurement is shown in Fig. S2(b). We note that the larger  $B_6^6$  term more thoroughly mixes the  $|\pm m_j\rangle$  CEF states which results in additional dipole-allowed transitions in the energy spectrum as shown in the inset of S2(b).

Using these parameters, one finds a continuous transition at 27.6 T along the easy (210) axis, and a first order transition at 30.7 T along the hard (100) axis. A quantum tricritical point (QTCP) occurs as the transverse field is rotated in the basal plane. If we take  $\phi = 0^\circ$  to correspond to the hard (100) axis the QTCP occurs at  $\phi = 5.5^\circ$ .

## EXTENDED HIGH-FIELD DATA ANALYSIS

### Analysis of raw pulsed field data

High-field magnetization measurements at Los Alamos were performed using a compensated coil extraction magnetometer. The crystal was mounted on a G-10 substrate to minimize the possible out-of plane misalignment and then placed in an ampoule which can be moved in and out of the coil without thermocycling. Two different crystal mountings were investigated with the field parallel to inequivalent (100) or (210) high-symmetry directions in hexagonal coordinates. The voltage induced in the coil by the field pulse is proportional to the sample susceptibility ( $dM/dH$ ). A peak in the raw  $dM/dH$  data indicates a phase transformation and the peak values are fit to obtain the critical field, as shown in Fig. S3. Magnetization [ $M(H)$ ] data are obtained by subtracting the empty

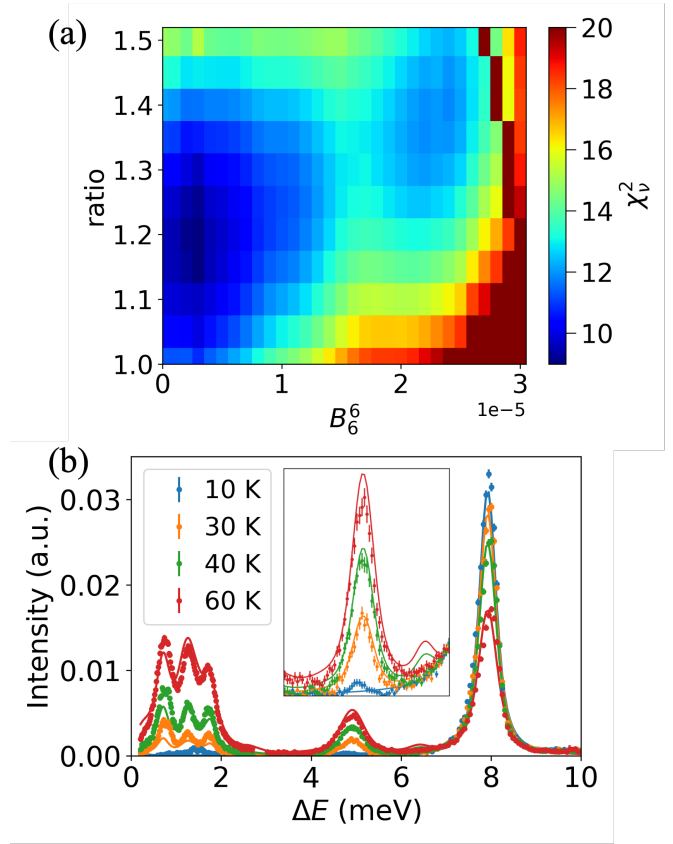


FIG. S2. (a) Reduced  $\chi_\nu^2$  map as a function of scaling ratio and  $B_6^6$  values that are fixed while fitting other CEF parameters. The global minimum (Case I) is found with ratio  $R = 1.2$  and  $B_6^6 = 3 \times 10^{-6}$  meV, and a local minimum (Case II) is found with  $R = 1.4$  and  $B_6^6 = 2.4 \times 10^{-5}$  meV. (b) The Case II parameters show the extra peaks in the spectrum. The insert shows the zoom-in between  $4 \text{ meV} < \Delta E < 7 \text{ meV}$  where Case II parameters predict an extra excitation that is not observed from INS measurements.

coil signal from the data with sample inside the coil and integrating with respect to field (time).

### Field rotation and PDO data

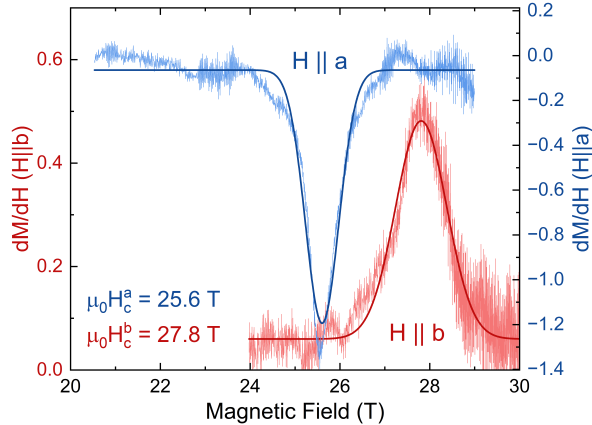
The proximity detector oscillator (PDO) measurements were performed at the Los Alamos pulsed field facility with fields up to 60 T at 0.6 K. The crystal was placed on top of a 10-turn coil made of 46-gauge copper wire, which is connected to the PDO circuit with resonant frequency in the range of 21 - 36 MHz. The technique is sensitive to changes of electrical conductivity and magnetic susceptibility:  $f \propto dM/dH$  [S4, S5]. The rf coil is mounted on goniometer enabling rotation about the coil axis at cryogenic temperatures. This configuration allows the in-plane orientation of applied field to be varied whilst measuring the transverse ( $c$ -axis component of) magnetic susceptibility.

Fig. S4(a) and (b) show PDO data for two different sample mountings as a function of planar rotation angle ( $\phi$ ) and

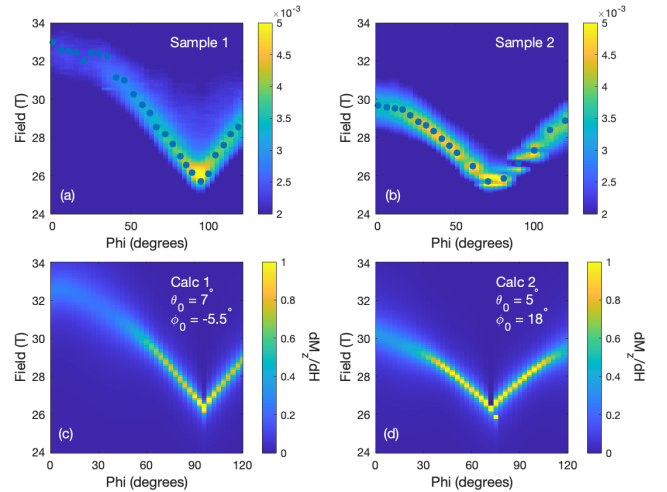


TABLE S1. Crystal-field eigenvalues and wavefunctions for TbV<sub>6</sub>Sn<sub>6</sub>.

| E (meV) | - 6)    | - 5)    | - 4)    | - 3)    | - 2)    | - 1)    | 0)      | 1)      | 2)      | 3)      | 4)      | 5)      | 6)      |
|---------|---------|---------|---------|---------|---------|---------|---------|---------|---------|---------|---------|---------|---------|
| Case I  |         |         |         |         |         |         |         |         |         |         |         |         |         |
| 0.000   | 0.7071  | 0.0     | 0.0     | 0.0     | 0.0     | 0.0     | 0.0048  | 0.0     | 0.0     | 0.0     | 0.0     | 0.0     | 0.7071  |
| 0.000   | -0.7071 | 0.0     | 0.0     | 0.0     | 0.0     | 0.0     | -0.0    | 0.0     | 0.0     | 0.0     | 0.0     | 0.0     | 0.7071  |
| 7.937   | 0.0     | -0.9998 | 0.0     | 0.0     | 0.0     | 0.0     | 0.0     | -0.0194 | 0.0     | 0.0     | 0.0     | 0.0     | 0.0     |
| 7.937   | 0.0     | 0.0     | 0.0     | 0.0     | 0.0     | 0.0194  | 0.0     | 0.0     | 0.0     | 0.0     | 0.0     | 0.9998  | 0.0     |
| 10.683  | -0.0034 | 0.0     | 0.0     | 0.0     | 0.0     | 0.0     | 1.0     | 0.0     | 0.0     | 0.0     | 0.0     | 0.0     | -0.0034 |
| 11.431  | 0.0     | -0.0194 | 0.0     | 0.0     | 0.0     | 0.0     | 0.0     | 0.9998  | 0.0     | 0.0     | 0.0     | 0.0     | 0.0     |
| 11.431  | 0.0     | 0.0     | 0.0     | 0.0     | 0.0     | 0.9998  | 0.0     | 0.0     | 0.0     | 0.0     | 0.0     | -0.0194 | 0.0     |
| 12.877  | 0.0     | 0.0     | 0.0     | 0.0     | -0.3674 | 0.0     | 0.0     | 0.0     | 0.0     | 0.0     | -0.93   | 0.0     | 0.0     |
| 12.877  | 0.0     | 0.0     | 0.93    | 0.0     | 0.0     | 0.0     | 0.0     | 0.0     | 0.3674  | 0.0     | 0.0     | 0.0     | 0.0     |
| 13.144  | 0.0     | 0.0     | 0.0     | 0.0     | 0.93    | 0.0     | 0.0     | 0.0     | 0.0     | 0.0     | -0.3674 | 0.0     | 0.0     |
| 13.144  | 0.0     | 0.0     | -0.3674 | 0.0     | 0.0     | 0.0     | 0.0     | 0.0     | 0.93    | 0.0     | 0.0     | 0.0     | 0.0     |
| 14.120  | 0.0     | 0.0     | 0.0     | -0.7071 | 0.0     | 0.0     | 0.0     | 0.0     | 0.0     | -0.7071 | 0.0     | 0.0     | 0.0     |
| 14.320  | 0.0     | 0.0     | 0.0     | 0.7071  | 0.0     | 0.0     | 0.0     | 0.0     | 0.0     | -0.7071 | 0.0     | 0.0     | 0.0     |
| Case II |         |         |         |         |         |         |         |         |         |         |         |         |         |
| 0.000   | 0.7068  | 0.0     | 0.0     | 0.0     | 0.0     | 0.0     | -0.0293 | 0.0     | 0.0     | 0.0     | 0.0     | 0.0     | 0.7068  |
| 0.010   | -0.7071 | 0.0     | 0.0     | 0.0     | 0.0     | 0.0     | -0.0    | 0.0     | 0.0     | 0.0     | 0.0     | 0.0     | 0.7071  |
| 7.932   | 0.0     | -0.995  | 0.0     | 0.0     | 0.0     | 0.0     | 0.0     | 0.0996  | 0.0     | 0.0     | 0.0     | 0.0     | 0.0     |
| 7.932   | 0.0     | 0.0     | 0.0     | 0.0     | 0.0     | -0.0996 | 0.0     | 0.0     | 0.0     | 0.0     | 0.0     | 0.995   | 0.0     |
| 11.870  | -0.0208 | 0.0     | 0.0     | 0.0     | 0.0     | 0.0     | -0.9996 | 0.0     | 0.0     | 0.0     | 0.0     | 0.0     | -0.0208 |
| 12.578  | 0.0     | -0.0996 | 0.0     | 0.0     | 0.0     | 0.0     | 0.0     | -0.995  | 0.0     | 0.0     | 0.0     | 0.0     | 0.0     |
| 12.578  | 0.0     | 0.0     | 0.0     | 0.0     | 0.0     | -0.995  | 0.0     | 0.0     | 0.0     | 0.0     | 0.0     | -0.0996 | 0.0     |
| 12.853  | 0.0     | 0.0     | 0.0     | 0.0     | -0.4758 | 0.0     | 0.0     | 0.0     | 0.0     | 0.0     | 0.8796  | 0.0     | 0.0     |
| 12.853  | 0.0     | 0.0     | 0.8796  | 0.0     | 0.0     | 0.0     | 0.0     | 0.0     | -0.4758 | 0.0     | 0.0     | 0.0     | 0.0     |
| 14.133  | 0.0     | 0.0     | 0.0     | -0.7071 | 0.0     | 0.0     | 0.0     | 0.0     | 0.0     | 0.7071  | 0.0     | 0.0     | 0.0     |
| 14.337  | 0.0     | 0.0     | -0.4758 | 0.0     | 0.0     | 0.0     | 0.0     | 0.0     | -0.8796 | 0.0     | 0.0     | 0.0     | 0.0     |
| 14.337  | 0.0     | 0.0     | 0.0     | 0.0     | 0.8796  | 0.0     | 0.0     | 0.0     | 0.0     | 0.0     | 0.4758  | 0.0     | 0.0     |
| 15.494  | 0.0     | 0.0     | 0.0     | 0.7071  | 0.0     | 0.0     | 0.0     | 0.0     | 0.0     | 0.7071  | 0.0     | 0.0     | 0.0     |

FIG. S3. Raw pulsed-field data proportional to  $dM/dH$  in the critical field region. Fits identify the critical field in the (100) and (210) directions.

field. Changes in the resonant frequency are associated with changes in the sample susceptibility,  $\chi_z = dM_z/dH$  such as that which occurs at the critical spin-reorientation field. For an ideally aligned sample, rotation would occur around the  $c$ -axis and PDO measurements would adopt a six-fold pattern of the critical field caused by the planar anisotropy parameter  $B_6^6$ . However, small tilts of the sample, which can be

FIG. S4. (a), (b) PDO data taken on two different samples with different tilt angles. Symbols are fits to the data at different  $\phi$  angles. (c), (d) MF calculations of  $dM_z/dH$  with angle misalignments,  $\theta_0$  and  $\phi_0$ , that best match the observed data.

imposed by large sample torque, will introduce a field component parallel to  $c$  that increases the apparent critical field. Such misalignment will lead to the observed two-fold pattern where the minimum critical field occurs for  $\phi$  angles where

the field does lie in the  $ab$  plane.

We can simulate the effect of sample tilt on the critical field using our magnetic Hamiltonian. Figures S4(c) and (d) show MF calculations of  $\chi_z = dM_z/dH$  for a misaligned sample as a function of rotation around an axis that is tilted from the crystallographic  $c$  axis by  $\theta_0$ . We introduce misalignment angles to mirror the observed data. The good agreement indicates that our samples are indeed misaligned to such a degree that we cannot determine  $B_6^6$  using this method. However, PDO does determine the minimum critical field that occurs at the one  $\phi$  angle where the field lies in the  $ab$  plane. This field (25.7 T) compares favorably to magnetization data shown in the main manuscript.

### Estimating CEF parameters from magnetization data

We can use the magnetization data to constrain our estimates of the CEF parameters. We start with the classical magnetic anisotropy energy (MAE)

$$E_A = K_1 \sin^2 \theta + K_2 \sin^4 \theta + K_3 \sin^6 \theta + K'_3 \sin^6 \theta \cos 6\varphi \quad (\text{S1})$$

where  $\theta$  and  $\varphi$  are the spherical angles describing the Tb moment direction. The MAE constants are related to the CEF parameters according to the following relationships

$$\begin{aligned} K_1 &= -3J^{(2)}B_2^0 - 40J^{(4)}B_4^0 - 168J^{(6)}B_6^0 & (\text{S2}) \\ K_2 &= 35J^{(4)}B_4^0 + 378J^{(6)}B_6^0 \\ K_3 &= -231J^{(6)}B_6^0 \\ K'_3 &= J^{(6)}B_6^0 \end{aligned}$$

where  $J^{(2)} = J(J - \frac{1}{2})$ ,  $J^{(4)} = J^{(2)}(J - 1)(J - \frac{3}{2})$ , and  $J^{(6)} = J^{(4)}(J - 2)(J - \frac{5}{2})$ . In a transverse field along  $x$ , the Zeeman energy is  $E_Z = -MH \sin \theta$  where  $M = 9 \mu_B$  is the full Tb moment. We can determine the equilibrium condition for the Tb angle by minimizing the total energy  $E = E_A + E_Z$ , leading to

$$2K_1 \sin \theta + 4K_2 \sin^3 \theta + 6(K_3 - |K'_3|) \sin^5 \theta - MH = 0 \quad (\text{S3})$$

For a small transverse field, the moment will tilt towards the field direction and the equilibrium condition for a small tilting angle is  $\theta \approx MH/2K_1$ . We can calculate the effective low-field transverse susceptibility in this limit as  $\chi_x = M_x/H = M^2/2K_1$ . Thus,  $\chi_x$  can be used to determine  $K_1$ . From fits to our DC susceptibility measurements, we estimate that  $\chi_x = 0.12 \mu_B/T$  which gives  $K_1 = 20$  meV. Note that for a uniaxial magnet in the absence of a molecular field, the main INS  $|6\rangle \rightarrow |5\rangle$  transition out of the ground state has an energy of  $\Delta \approx 2K_1/J = 7.9$  meV and from this we estimate that  $K_1 = 23.7$  meV.

We can also study the equilibrium condition that leads to the magnetization jump at a critical field  $H_c$  where the moment

lies fully in the plane. At  $H_c$ , the energy at the critical angle  $\theta_c$  is equal to the energy of the in-plane state with  $\theta = \pi/2$ .

$$\begin{aligned} K_1 \sin^2 \theta_c + K_2 \sin^4 \theta_c + (K_3 - |K'_3|) \sin^6 \theta_c & \\ - MH_c \sin \theta_c - (K_1 + K_2 + K_3 - |K'_3| - MH_c) = 0 & \end{aligned} \quad (\text{S4})$$

Here, we can use the experimental values of  $K_1$  and  $H_c$  as constraints to numerically solve Eqns. S3 and S4 for  $\theta_c$ ,  $B_4^0$ , and  $B_6^0$  while letting  $B_6^6 = 0$ . To do this, we also need another equation. We can use the relation for the  $|5\rangle \rightarrow |4\rangle$  energy splitting  $\Delta' = 4.9$  meV.

$$\begin{aligned} \Delta' &= -3B_2^0(2J - 3) - 40B_4^0(2J - 3)(J - 1)(J - 5) & (\text{S5}) \\ &- 42B_6^0(2J - 5)(2J - 3)(J - 2)(J - 1)(2J - 21) \end{aligned}$$

Using the three observables ( $K_1 = 23.7$  meV,  $\mu_0 H_c = 25.6$  T, and  $\Delta' = 4.9$  meV), we simultaneously solve the three equations to obtain;  $\sin \theta_c = 0.297$ ,  $B_4^0 = -6.16 \times 10^{-4}$  meV, and  $B_6^0 = 2.43 \times 10^{-6}$  meV. We also use the  $K_1$  constraint to obtain  $B_2^0 = -0.0975$  meV. These values are very similar to the CEF parameters obtained from fitting the INS data directly.

## EXTENDED THEORY AND MODELING

### Hyperfine interactions

Terbium has a single stable isotope with nuclear spin  $I = 3/2$ . The strength of the hyperfine interaction,  $H_{hyp} = \mathbf{AI} \cdot \mathbf{J}$ , is  $A = 25.4$  mK [S6]. For comparison, the strongest rare-earth hyperfine interaction is in holmium with  $A = 39$  mK and  $I = 7/2$ , which leads to substantial corrections to the low-temperature phase diagram of LiHoF<sub>4</sub> [S7]. The strong Ising anisotropy of LiHoF<sub>4</sub> through the critical transverse field leads to a strongly anisotropic effective hyperfine interaction [S8–S10]. In TbV<sub>6</sub>Sn<sub>6</sub>, the anisotropy of the system evolves with the transverse field, and with the INS-derived CEF parameters, the system loses its strong Ising character around 25 T, just below the critical transverse field [see Fig. S6 (inset)], which means the hyperfine corrections to the TbV<sub>6</sub>Sn<sub>6</sub> phase diagram are small, with the increase of the critical field at  $T = 0$  K being  $\sim 0.1\%$ .

### Dipolar interactions

The dipole-dipole interactions between Tb moments are

$$\mathcal{H}_{dip} = -\frac{\mathcal{J}_D}{2} \sum_{i \neq j} \sum_{\mu\nu} D_{ij}^{\mu\nu} J_i^\mu J_j^\nu, \quad (\text{S6})$$

where

$$D_{ij}^{\mu\nu} = \frac{1}{r_{ij}^3} \left( \frac{3r_{ij}^\mu r_{ij}^\nu}{r_{ij}^2} - \delta_{\mu\nu} \right) \quad (\text{S7})$$

and  $\mathcal{J}_D = \mu_0(g_J\mu_B)^2/(4\pi)$ . Note that at zero wave-vector the off-diagonal components of the dipolar sums vanish due to the lattice symmetry so that these terms may be neglected in mean-field calculations. The Tb are situated on triangular lattices in the basal plane, with the lattice spacing at  $T = 10$  K being  $a = b = 5.512 \text{ \AA}$  and  $c = 9.166 \text{ \AA}$  [S11], leading to a spin density,  $\rho_s = 4.146 \times 10^{27} \text{ Tb/m}^3$ . Dipolar interactions on this lattice favor antiferromagnetic alignments, with a characteristic strength,  $\rho_s \mathcal{J}_D = 5.8 \text{ mK}$ , while the spins experimentally order ferromagnetically at  $T_C \approx 4.4 \text{ K}$  [S11], indicating that the dominant coupling between spins is not dipolar, but instead indirect exchange mediated by the vanadium conduction electrons.

### Field-Temperature Phase Diagram

At sufficiently high temperatures, the mean-field (MF) phase transition is second order, with a classical tricritical point (TCP) at  $T_{tcp} = 1.65 \text{ K}$  along the hard, (100) axis and  $T_{tcp} = 1 \text{ K}$  along the easy, (210) axis for the small (Case I)  $B_6^6$  CEF parameters. The tricritical point leads to a wing structure [S12] in small  $c$ -axis fields. This wing structure is very compact, with quantum critical end points at  $(B_x, B_z) \approx (27, \pm 0.2) \text{ T}$  along the hard, (100) axis, as shown in Fig. S5.

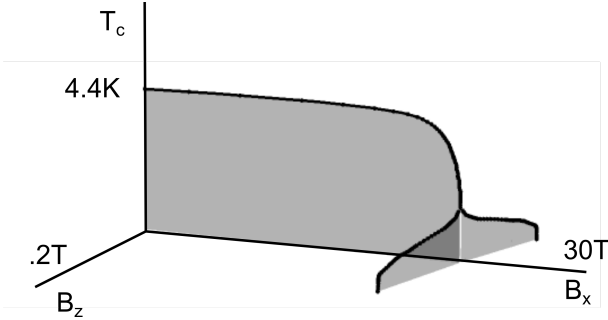


FIG. S5. MF phase diagram of  $\text{TbV}_6\text{Sn}_6$  in temperature ( $T$ ), transverse field along the hard, (100) axis,  $B_x$  and longitudinal field,  $B_z$ . This calculation uses the Case I CEF parameters from the main text and an interaction strength,  $\mathcal{J}_0 = 122 \text{ mK}$ . At low temperatures, the transition is first order, with  $T_{TCP} = 1.65 \text{ K}$ , above which it is continuous. There is a very narrow wing structure, with quantum critical end points in the  $(B_x, B_z)$  plane at  $\approx (27, \pm 0.2) \text{ T}$ .

### Effective spin-1/2 Ising model

When the ground-state doublet is well separated from the excited crystal-field levels, one may truncate the full Hamiltonian to obtain an effective low energy spin-1/2 model

[S8, S13]. This procedure works well for most of the low-temperature region of the phase diagram, but breaks down in the vicinity of the critical field where there is strong mixing between the low-energy doublet and the third CEF level (see Figs. ?? and ??), as the effective spin-1/2 model predicts a continuous transition where the full Hamiltonian may give either order, depending on the parameters and field direction.

We apply this procedure to diagonalize Eqn. ??, finding  $\mathcal{H}_0 = \mathcal{H}_{\text{CEF}}(\mathbf{J}) - g_J\mu_B B_x J^x$ , where the effective spin-1/2 operators are  $J^\mu = C_\mu + C_{\mu\mu}\sigma^\mu$ ;  $\sigma^\mu$  are Pauli matrices. Here,  $C_y = C_z = 0$ , and  $J^x = C_x + C_{xx}\sigma^x$  captures fluctuations about a permanent field-induced moment along  $\hat{x}$ .

We obtain the effective low-temperature spin-1/2 model,

$$\mathcal{H} = -\frac{1}{2} \sum_{ij,\alpha} V_{ij}^{\alpha\alpha} S_i^\alpha S_j^\alpha - (\Delta_x + 2\mathcal{J}_0 C_x C_{xx}) \sum_i S_i^x, \quad (\text{S8})$$

where  $S_i^\alpha = \sigma_i^\alpha/2$  are spin-1/2 operators,  $V_{ij}^{\alpha\alpha} = 4C_{\alpha\alpha}^2(B_x)\mathcal{J}_{ij}$ , and  $\Delta_x(B_x)$  is the splitting of the ground state doublet. The interaction leads to an effective transverse field,  $\tilde{\Delta}_x = \Delta_x + 2\mathcal{J}_0 C_x C_{xx}$ . At transverse fields below  $B_x = 25 \text{ T}$ , the system has a strong Ising anisotropy ( $C_{zz} \approx 6$ , and  $C_{xx} \approx C_{yy} \approx 0$ ), and the Hamiltonian reduces to the TFIM

$$\mathcal{H} = -\frac{1}{2} \sum_{ij} V_{ij}^{zz} S_i^z S_j^z - \Delta_x \sum_i S_i^x. \quad (\text{S9})$$

For larger transverse fields, the system is better described as an anisotropic Heisenberg magnet. orientation in the basal plane.

Fig. S6 compares the MF magnetizations determined by the full CEF Hamiltonian versus the truncated model, for the Case I CEF parameters (small  $B_6^6$ ) with the field along the hard axis and  $\mathcal{J}_0 = 0.122 \text{ K}$ . The agreement is good, except very close to the transition, and the system clearly loses its Ising nature above the transition. The results with the field along the easy axis are similar.

### Sample tilt and magnetization

The ‘‘transverse’’ magnetization measurements presented in the body of the paper are magnetizations measured in the direction of the applied field. With perfect sample alignment, one may neglect transverse demagnetization field effects in thin plate-like samples of  $\text{TbV}_6\text{Sn}_6$  ( $N^\perp \approx 0$ ). However, the sample may experience strong magnetic torques and imperfect alignment, causing the applied field to have a small longitudinal component. In this case, domain structure and demagnetization fields must be accounted for.

Consider a tilted sample with  $\mathbf{n} = (\sin\theta_0 \cos\phi_0, \sin\theta_0 \sin\phi_0, \cos\theta_0)$  perpendicular to the  $ab$ -plane. The effect of the applied field in the sample frame is,

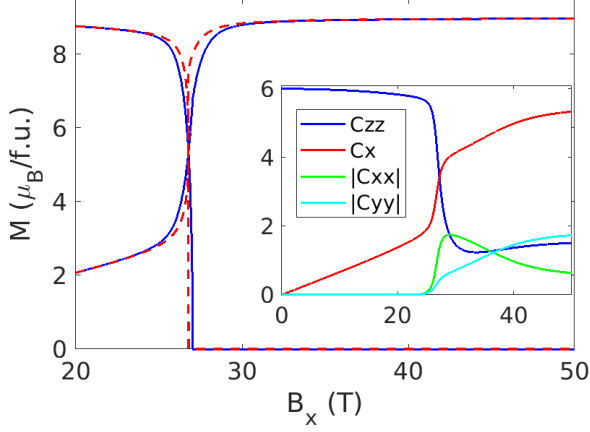


FIG. S6. Longitudinal and transverse MF magnetization at  $T = 0$  determined by the full Hamiltonian (dashed, red lines) and the truncated Hamiltonian (solid, blue lines) for the Case I (small  $B_6^6$ ) CEF parameters with the transverse field along the hard (100) axis and  $\mathcal{J}_0 = 0.122$  K. The truncated Hamiltonian erroneously gives a continuous transition, which is first order in the full model. The inset shows the evolution of the truncation parameters in a transverse field.

$$B_x = B[\cos \theta_0 + \sin^2 \phi_0(1 - \cos \theta_0)] \quad (\text{S10})$$

$$B_y = -B \sin \phi_0 \cos \phi_0(1 - \cos \theta_0)$$

$$B_z = B \cos \phi_0 \sin \theta_0$$

If faceting on the sample surface allows for good alignment in the planes, we may assume either  $\phi_0 = \pi/2$  or  $\phi_0 = 0$ , giving sample frame fields of  $\mathbf{B} = B(1, 0, 0)$  or  $\mathbf{B} = B(\cos \theta_0, 0, \sin \theta_0)$ , respectively. We assume  $\phi_0 = 0$ , giving the “transverse” field a longitudinal component.

Domain structure forms to minimize the magnetostatic energy of a sample. In Ising magnets with highly mobile domain walls, the average internal field is empirically  $\bar{H}_{in}^z = H_a^z - N^z \bar{M}^z \approx 0$  [S14, S15], where  $\bar{M}^z$  is the average magnetization of the sample and  $N^z$  is its demagnetization factor. The experimental susceptibility of a multidomain sample is then  $\chi_{exp}^{zz} = \bar{M}^z / H_a^z = 1/N^z$ . The finite energy of the domain walls, and pinning potentials, will modify this result. In a plate-like sample with  $N^z \approx 1$  and highly mobile domain walls with negligible wall energies, we expect  $H_a^z \approx \bar{M}^z$  up to the saturation value of the magnetization,  $M^z(T, B_x)$ . In  $\text{TbV}_6\text{Sn}_6$ ,  $\mu_0 \mathbf{M} = 0.0725 \langle \mathbf{J} \rangle$  Tesla. When the spins are fully polarized ( $\langle J^z \rangle \approx 6$  at  $T = 0$  K and  $B_x = 0$  T), this gives a saturation field of  $B_z = 0.4$  T.

In Fig. S7(a) we show the MF magnetization using the Case I CEF parameters (small  $B_6^6$ ) with  $\mathcal{J}_0 = 0.122$  K at  $T = 0.625$  K. The applied field is along the hard axis assuming a  $\theta_0 = 2^\circ$  sample tilt. The solid lines show the transverse magnetization and the magnetization in the direction of the applied field, which have a low-field slope of  $0.1 \mu_B/\text{T}$ . If we account for domains, we should take the longitudinal component of the magnetization to be the minimum of  $\langle J^z \rangle_{MF}$

and  $\langle J^z \rangle = \mu_0 \bar{M}^z / 0.0725 = B^z / 0.0725$ , which gives the dashed line. Its low field slope is  $0.12 \mu_B/\text{T}$ , in better agreement with the experimental value. Increasing the sample tilt leads to a steeper rise in the low-field magnetization that is less consistent.

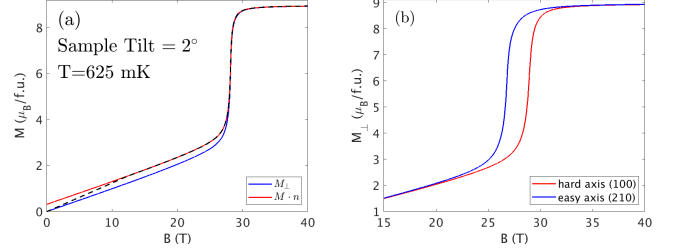


FIG. S7. Effect of sample tilt and domain structure on the MF magnetization, calculated for the Case I CEF parameters at  $T = 0.625$  K and with  $\mathcal{J}_0 = 0.122$  K to give the experimental  $T_C$ . (a) The MF magnetization along the actual transverse direction,  $M_\perp$  and the tilted applied field direction,  $\mathbf{M} \cdot \mathbf{n}$  with a  $2^\circ$  sample tilt; the field is primarily along the hard (100) axis. The dashed line shows the magnetization when  $M^z$  is the minimum of either its MF value or  $\bar{M}^z$ , the average longitudinal magnetization accounting for domain structure. (b) Easy (210) and hard (100) transverse magnetization curves assuming a  $2.5^\circ$  tilt between measurements. The easy (hard) axes calculations assume an out of plane tilt of  $0.5^\circ$  ( $3^\circ$ ) in order to roughly mimic Fig. 2(a) in the main text.

The calculated curves, with an identical sample tilt along both the easy and hard axes are inconsistent with the measured magnetizations. In order to obtain the  $\approx 2.2$  T separation of the magnetization curves seen experimentally, we must either increase the value of  $B_6^6$  or assume the sample tilt changes between the easy and hard axis measurements. In Fig. S7(b), we use the Case I CEF parameters to calculate the magnetizations assuming a relative  $2.5^\circ$  tilt between measurements, which reproduces the experimental magnetization curves in Fig. ?? reasonably well; however, if one considers the magnetization in the direction of the applied field, rather than just  $M_\perp$ , and accounts for domain structure, the agreement is not as good. In particular, we expect the slope of the low-field magnetization to vary with the sample tilt; this is not seen in the experimental data, but it is possible that the sample only tilts or twists out of alignment at high fields.

Similar magnetization curves to those shown in Fig. S7 can be produced if  $B_6^6 = 5 \times 10^{-6}$  meV, above the QTCP threshold, but there are substantial discrepancies if  $B_6^6$  is increased above this value. With the field along the easy axis, the rise in the magnetization near the phase transition is less steep than what is observed experimentally. Along the hard axis, the magnetization rises more steeply, cutting through the easy axis curve (as in Fig. ??). It takes a substantial sample tilt to eliminate this crossing, and the separation of the two curves is larger than what is measured experimentally.

## DENSITY-FUNCTIONAL THEORY CALCULATIONS

Given the challenges in experimentally determining  $B_6^6$ , we conducted density-functional theory (DFT) calculations to estimate this parameter. The ab initio estimation of CEF parameters is generally challenging in MF methods like DFT, as the  $4f$  self-interaction in DFT is at least an order of magnitude larger than the crystal field strength itself. In this study, we employed a recently proposed total-energy-mapping method that leverages the invariance of the orbital dependence of self-interaction errors [S16].

For the hexagonal system with  $C_{3v}$  point-group symmetry at the  $R$  site, the in-plane anisotropy within CEF theory depends solely on  $B_6^6$ .

$$E(\phi, \theta = \frac{\pi}{2}) = \frac{1}{16} B_6^6 \langle \mathcal{O}_6^6 \rangle \cos 6\phi \quad (\text{S11})$$

Here, the nearest  $R$ - $V$  bond direction in the basal plane is along the  $[210]$  direction (defined as  $\phi = 0$ ), while the nearest  $\text{Tb}$ - $\text{Tb}$  is along the  $[100]$  direction ( $\phi = -\pi/6$ ). We calculated the total energy difference between these two directions,  $\Delta E = E_{210} - E_{100}$ , to extract the anisotropy and determine  $B_6^6$ .

Self-consistent DFT+ $U$  calculations, including spin-orbit coupling, were performed. A sufficiently large  $U$  value is necessary to push the  $4f$  states deeper away from the Fermi level. This ensures that the calculations converge to the Hund's rule ground state of  $\text{Tb}^{3+}$ , consistent with experimental results, avoiding the unphysical DFT+ $U$  ground state of  $|m_l^\downarrow = 2\rangle$  caused by the orbital dependence of self-interaction errors [S16]. This approach has been shown to accurately reproduce results for all existing  $\text{RMn}_6\text{Sn}_6$  compounds and other well-studied rare-earth-containing isostructural materials. Further details of the DFT+ $U$  calculations are available in other sources.

The calculated energy difference at  $U=10$  eV is  $\Delta E = 0.408$  meV, yielding a  $B_6^6$  of  $2.08 \times 10^{-5}$  meV, which aligns closely with the  $B_6^6$  value of the Case II (larger) experimental set. We also explored the sensitivity of  $B_6^6$  to the  $U$  parameter. Across a reasonable range of  $U$  values of 6–12 eV,  $B_6^6$  varies from  $1.67 \times 10^{-5}$  to  $2.77 \times 10^{-5}$  meV. These DFT+ $U$  calculations are consistent with the experimental data, supporting the presence of a sizable  $B_6^6$ .

growth of single crystalline samples, Philosophical Magazine **96**, 84 (2016).

- [S4] M. Altarawneh, C. Mielke, and J. S. Brooks, Proximity detector circuits: An alternative to tunnel diode oscillators for contactless measurements in pulsed magnetic field environments, Rev. Sci. Instrum. , 066104 (2009).
- [S5] e. a. S. Ghannadzadeh, Measurement of magnetic susceptibility in pulsed magnetic fields using a proximity detector oscillator, Rev. Sci. Instrum. , 113902 (2011).
- [S6] B. Bleaney and R. W. Hill, Hyperfine Structure in Terbium Metal, Proc. Phys. Soc. **78**, 313 (1961).
- [S7] D. Bitko, T. F. Rosenbaum, and G. Aeppli, Quantum Critical Behavior for a Model Magnet, Phys. Rev. Lett. **77**, 940 (1996).
- [S8] P. B. Chakraborty, P. Henelius, H. K. A. W. Sandvik, and S. M. Girvin, Theory of the magnetic phase diagram of  $\text{LiHoF}_4$ , Phys. Rev. B **70**, 144411 (2004).
- [S9] M. Schechter and P. C. E. Stamp, Derivation of the low-T phase diagram of  $\text{LiHo}_x\text{Y}_{1-x}\text{F}_4$ : A dipolar quantum Ising magnet, Phys. Rev. B **78**, 054438 (2008).
- [S10] R. D. McKenzie and P. C. E. Stamp, Thermodynamics of a quantum Ising system coupled to a spin bath, Phys. Rev. B **97**, 214430 (2018).
- [S11] G. Pokharel, B. Ortiz, J. Chamorro, P. Sarte, L. Kautzsch, G. Wu, J. Ruff, and S. D. Wilson, Highly anisotropic magnetism in the vanadium-based kagome metal  $\text{TbV}_6\text{Sn}_6$ , Phys. Rev. Mater. **6**, 104202 (2022).
- [S12] R. B. Griffiths, Thermodynamics Near the Two-Fluid Critical Mixing Point in  $\text{He}^3$ - $\text{He}^4$ , Phys. Rev. Lett. **24**, 715 (1970).
- [S13] S. Tabei, M. Gingras, Y. Kao, and T. Yavors'kii, Perturbative quantum Monte Carlo study of  $\text{LiHoF}_4$  in a transverse magnetic field, Phys. Rev. B **78**, 184408 (2008).
- [S14] A. H. Cooke, D. A. Jones, J. F. A. Silva, and M. R. Wells, Ferromagnetism in lithium holmium fluoride- $\text{LiHoF}_4$ : I. Magnetic measurements, J. Phys. C: Solid State Phys. **8**, 4083 (1975).
- [S15] G. Mennenga, L. J. de Jongh, and W. J. Huiskamp, Field Dependent Specific Heat Study of the Dipolar Ising Ferromagnet  $\text{LiHoF}_4$ , Journal of Magnetism and Magnetic Materials **44**, 59 (1984).
- [S16] Y. Lee, Z. Ning, R. Flint, R. J. McQueeney, I. I. Mazin, and L. Ke, Toward a first-principles theory of rare-earth ions in crystals, arXiv:2407.10067 (2024)

- 
- [S1] E. Rosenberg, J. M. DeStefano, Y. Guo, J. S. Oh, M. Hashimoto, D. Lu, R. J. Birgeneau, Y. Lee, L. Ke, M. Yi, and J.-H. Chu, Uniaxial ferromagnetism in the kagome metal  $\text{TbV}_6\text{Sn}_6$ , Phys. Rev. B **106**, 115139 (2022).
  - [S2] X. Zhang, Z. Liu, Q. Cui, Q. Guo, N. Wang, L. Shi, H. Zhang, W. Wang, X. Dong, J. Sun, Z. Dun, and J. Cheng, Electronic and magnetic properties of intermetallic kagome magnets  $\text{RV}_6\text{Sn}_6$  ( $R = \text{Tb}-\text{Tm}$ ), Phys. Rev. Mater. **6**, 105001 (2022).
  - [S3] P. C. Canfield, T. Kong, U. S. Kaluarachchi, and N. H. Jo, Use of frit-disc crucibles for routine and exploratory solution